

Observation of orbital pumping

Hiroki Hayashi,^{1,2} Dongwook Go,^{3,4} Yuriy Mokrousov,^{3,4} and Kazuya Ando^{a1,2,5}

¹*Department of Applied Physics and Physico-Informatics,*

Keio University, Yokohama 223-8522, Japan

²*Keio Institute of Pure and Applied Science,*

Keio University, Yokohama 223-8522, Japan

³*Peter Grünberg Institut and Institute for Advanced Simulation,*

Forschungszentrum Jülich and JARA, 52425 Jülich, Germany

⁴*Institute of Physics, Johannes Gutenberg University Mainz, 55099 Mainz, Germany*

⁵*Center for Spintronics Research Network,*

Keio University, Yokohama 223-8522, Japan

^a Correspondence and requests for materials should be addressed to ando@appi.keio.ac.jp

Abstract

Harnessing spin and orbital angular momentum is a fundamental concept in condensed matter physics, materials science, and quantum-device applications. In particular, the search for phenomena that generate a flow of spin angular momentum, a spin current, has led to the development of spintronics, advancing the understanding of angular momentum dynamics at the nanoscale. In contrast, the generation of an orbital current, the orbital counterpart of a spin current, remains a significant challenge. Here, we report the observation of orbital-current generation from magnetization dynamics: orbital pumping. We show that the orbital pumping in Ni/Ti bilayers injects an orbital current into the Ti layer, which is detected through the inverse orbital Hall effect. The orbital pumping is the orbital counterpart of the spin pumping, which is one of the most versatile and powerful mechanisms for spin-current generation. Our findings provide a promising approach for generating orbital currents, opening the door to explore the orbital analogue of spintronics: orbitronics.

Main

Electrons carry spin and orbital angular momentum, both of which are fundamental to the electronic and magnetic properties of materials. Over the past three decades, studies of a flow of spin angular momentum, a spin current, have revealed its fascinating topological, relativistic, and quantum mechanical nature, leading to the development of spintronics. The key element of spintronics is the interplay between spin currents and magnetization in ferromagnetic/nonmagnetic (FM/NM) bilayers¹. In a FM/NM bilayer, when a spin current is injected into the FM layer from the adjacent NM layer, the injected spin current interacts with the magnetization through the exchange coupling in the FM layer, exerting a torque, called a spin torque, on the magnetization². The spin torque drives domain-wall motion, magnetization switching, and magnetization precession, providing a way to realize a plethora of ultralow power and fast spintronic devices, such as nonvolatile magnetic memories, nanoscale microwave sources, and neuromorphic computing devices³⁻⁵. The reciprocal effect of the spin torque is known as the spin pumping, a phenomenon in which precessing magnetization in the FM layer pumps a spin current into the adjacent NM layer⁶⁻⁸. The spin pumping is one of the most versatile and powerful mechanisms for spin-current generation,

leading to the discovery of a variety of spin-current phenomena, such as spin transport in insulators and nonvolatile electric control of spin-charge conversion⁹⁻¹¹. This pair of reciprocal effects, the spin torque and the spin pumping, has played a central role in the development of modern spintronics.

In contrast to the success in establishing the physics of spin currents, the orbital counterpart of spin currents, orbital currents, has been largely overlooked. Recent studies, however, have suggested the crucial role of orbital currents, a flow of orbital angular momentum, in the dynamics of angular momentum in solids^{12,13}. In particular, experimental and theoretical studies have suggested the existence of the orbital counterpart of the spin torque: an orbital torque¹⁴⁻²³. The orbital torque emerges when an orbital current is injected into a FM layer. In the FM layer, the injected orbital angular momentum interacts with the magnetization through a combined action of the spin-orbit coupling and the exchange coupling in the FM layer, exerting a torque on the magnetization, which is the orbital torque¹⁴. The Onsager's reciprocal relations guarantee the existence of the reciprocal effect of the orbital torque, in which an orbital current is pumped by magnetization dynamics. This phenomenon is the orbital counterpart of the spin pumping and can be referred to as orbital pumping. Despite its importance, however, the orbital pumping remains unexplored; the orbital pumping is the missing piece in the set of spin and orbital current phenomena (see Fig. 1a).

In this work, we report the observation of the orbital pumping. We show that a charge current is generated at ferromagnetic resonance (FMR) in Ni/Ti bilayers, in which the existence of the orbital torque originating from the orbital Hall effect (OHE) is well established²². In FM/NM bilayers, the precession of the magnetization in the FM layer can generate charge currents in the NM layer through two distinct channels: the spin pumping followed by the inverse spin Hall effect (ISHE) and the orbital pumping followed by the inverse orbital Hall effect (IOHE). We demonstrate that the experimental characteristics of the observed current are consistent with it being generated through the IOHE induced by the orbital pumping.

The orbital pumping can be understood as an orbital analog of the spin pumping⁷ with the same symmetry constraint (the physical picture is explained in Supplementary Note 1). In a NM/FM bilayer, an orbital current driven by dynamics of the magnetization is given by

$$\mathbf{j}_o = \beta \mathbf{m} \times \frac{d\mathbf{m}}{dt} + \beta' \frac{d\mathbf{m}}{dt}, \quad (1)$$

where \mathbf{m} denotes the unit vector of the magnetization. Here, the orbital polarization direc-

tion of \mathbf{j}_o is represented by its vector direction, and the propagation direction of electrons is perpendicular to the interface. However, the crucial difference between the orbital pumping and the spin pumping is that the orbital pumping requires the spin-orbit coupling in its microscopic mechanism²⁴. This is because the orbital angular momentum interacts with the magnetization only indirectly via the spin-orbit interaction^{14,25}. Therefore, the orbital pumping sensitively depends on how the spin and orbital degrees of freedom are correlated, which differs from material to material²⁴. A recent theory predicts that ferromagnetic Ni exhibits the strongest orbital pumping among Fe, Co, and Ni²⁴. It has been found that Ni exhibits pronounced correlation between the spin and orbital angular momenta near the Fermi surface^{20,24,25}.

As schematically illustrated in Fig. 1a, the orbital pumping can be electrically detected by the IOHE, as the spin pumping is detected by the ISHE. Here, the major difference between the IOHE and ISHE is their dependence on the spin-orbit coupling. While the ISHE arises from the spin-orbit coupling, the IOHE does not require it. Thus, a light metal such as Ti can be used to detect the orbital pumping. We note that recent experiments have revealed large OHE in Ti^{21,22}. To detect the spin pumping, on the other hand, typically a heavy metal such as Pt is employed for its large ISHE. This motivates us to consider the Ti/Ni bilayers, in which gigantic orbital torque response has been observed in the previous work²².

Charge-current generation

To detect the orbital pumping, we measured the direct-current (DC) voltage V_{DC} generated at the FMR for FM/NM bilayers with FM = Ni, Fe, or Co and NM = Ti or Pt. In Fig. 1b, we show a schematic of the device and experimental setup (for details, see Methods). Equation (1) shows that the DC component of an orbital current generated by the orbital pumping is proportional to the projection of $\mathbf{m} \times d\mathbf{m}/dt$ onto the magnetization-precession axis. This projection is proportional to the square of the magnetization-precession amplitude, showing that the injected orbital current is proportional to the microwave power P_{in} and microwave absorption intensity P (see also Supplementary Note 2). Equation (1) also shows that the orbital polarization direction of the DC component of the injected orbital current is directed along the magnetization-precession axis, which is parallel to an external magnetic field in the FM/NM bilayers at the FMR. For the measurement, we applied a radio frequency (RF)

current I_{RF} with a frequency of f perpendicular to the direction across electrodes attached to the FM/NM device and swept an in-plane external field H applied at an angle of θ from the direction of the applied RF current (see Fig. 1b).

In Fig. 1c, we show magnetic field H dependence of the microwave absorption P and charge current $I_{\text{DC}} = V_{\text{DC}}/R$ signals measured for the Ni(5 nm)/Ti(10 nm) bilayer at $\theta = 0$, where R is the resistance of the device between the electrodes, and the numbers in parentheses represent the thickness. Figure 1c shows that despite the negligible ISHE in the Ti layer²⁶, a clear I_{DC} signal appears around the FMR field H_{FMR} . The observed charge-current signal can be decomposed into symmetric and antisymmetric functions with respect to H_{FMR} : $I_{\text{DC}} = I_{\text{sym}}W^2/[(\mu_0H - \mu_0H_{\text{FMR}})^2 + W^2] + I_{\text{antisym}}W(\mu_0H - \mu_0H_{\text{FMR}})/[(\mu_0H - \mu_0H_{\text{FMR}})^2 + W^2]$, where W denotes the FMR linewidth²⁷. The spin and orbital pumping generate the symmetric component I_{sym} through the ISHE and IOHE, respectively, because the DC component of the pumped current is proportional to the microwave absorption intensity²⁸. Figure 1c shows that the I_{DC} signal in the Ni/Ti bilayer is dominated by the symmetric component I_{sym} , suggesting that the observed charge current stems from the orbital pumping. Here, in the I_{DC} signal, the nonzero antisymmetric component I_{antisym} arises from spin rectification effects, which can be induced by the anisotropic magnetoresistance (AMR), the planar Hall effect (PHE), and the anomalous Hall effect (AHE) in the Ni layer^{29,30}. The asymmetric line shape in the P signal is presumably induced by eddy currents, which lead to an absorption-dispersion admixture³¹.

To reveal the origin of the charge current observed in the Ni/Ti bilayer, we measured the microwave absorption P and the charge current I_{DC} for Ni(5 nm) and Fe(5 nm)/Ti(10 nm) films, as well as the Ni(5 nm)/Ti(10 nm) bilayer at various frequencies f . Figures 2a-2c show the H dependence of P and $I_{\text{DC}}/P_{\text{abs}}$ for the three devices at $\theta = 0$, where P_{abs} is the microwave absorption intensity at the FMR field (see Fig. 1c). We note that the symmetric component of $I_{\text{DC}}/P_{\text{abs}}$, $I_{\text{sym}}/P_{\text{abs}}$, in the Ni single-layer film is negligible compared to that in the Ni/Ti bilayer (see Figs. 2a and 2b). This result demonstrates that the I_{sym} signal in the Ni/Ti bilayer is generated in the Ti layer; spin-rectification effects and thermoelectric effects in the Ni layer are not the source of the observed I_{sym} signals in the Ni/Ti bilayer. The contribution from the charge current generated in the Ni layer is discussed in detail in Supplementary Note 3.

An important feature of the I_{sym} signal is that its magnitude strongly depends on the

choice of the FM layer. Figure 2c shows that $I_{\text{sym}}/P_{\text{abs}}$ is vanishingly small in the Fe/Ti bilayer, despite the fact that the I_{sym} signal in the Ni/Ti bilayer originates from the Ti layer. The distinct difference in the magnitude of $I_{\text{sym}}/P_{\text{abs}}$ between the Ni/Ti and Fe/Ti bilayers is the key feature of the orbital pumping²⁴. In Ni, the electronic occupation of the d orbital shells is optimized such that the spin-orbit correlation is particularly strong near the Fermi energy^{20,22,25}. The strong spin-orbit correlation near the Fermi energy results in the strong coupling between the magnetization and orbital current in Ni, which has been confirmed by the orbital-torque studies^{19,20,22,23}. This implies a large orbital pumping efficiency β in the Ni/Ti bilayer (see Eq. (1)), suggesting that the orbital pumping in the Ni/Ti bilayer can inject a large orbital current into the Ti bilayer. In contrast, we expect that the orbital pumping in the Fe/Ti bilayer is inefficient. The reason for this is that the spin-orbit correlation near the Fermi energy in Fe is much smaller than that in Ni, as the hotspots for the spin-orbit correlation are located about 1 eV below the Fermi energy in Fe²⁵. The inefficient coupling between the magnetization and orbital current in Fe has been demonstrated in previous reports; while the current-induced torques in Ni-based structures are dominated by the orbital torques, the spin torques provide the dominant contribution in Fe-based structures^{20,22}. This indicates that the distinct difference in the observed charge-current signals between the Ni/Ti and Fe/Ti bilayers can be primarily attributed to the large difference in the orbital pumping efficiency β due to the different strengths of the spin-orbit correlation near the Fermi energy between Ni and Fe (see also Supplementary Note 1).

We have confirmed that the f dependence of $I_{\text{sym}}/P_{\text{abs}}$ of the Ni/Ti bilayer is consistent with the model of the spin and orbital pumping (see Supplementary Note 4). Here, the negligible $I_{\text{sym}}/P_{\text{abs}}$ in the Fe/Ti bilayer indicates that the charge current due to the ISHE is negligible in the FM/Ti bilayers. This result is consistent with the vanishingly small spin Hall angle of Ti²⁶, $\theta_{\text{SH}} = -3.6 \times 10^{-4}$, which is three orders of magnitude smaller than that of Pt. The negligible $I_{\text{sym}}/P_{\text{abs}}$ in the Fe/Ti bilayer also supports that sample heating is irrelevant to the charge-current signals observed in the Ni/Ti bilayer because thermoelectric effects are comparable between Fe and Ni³².

Characterization of charge current

To obtain further evidence for the IOHE induced by the orbital pumping, we measured I_{DC} for the Ni/Ti bilayer by varying the microwave power P_{in} and magnetic field angle θ .

In Fig. 3a, we show the I_{DC} spectra for the Ni/Ti bilayer measured at different P_{in} with applying the magnetic field at $\theta = 0$ and $\theta = 180^\circ$. By fitting the spectra using the sum of the symmetric and antisymmetric functions, we obtain the P_{in} dependence of I_{sym} , as shown in Fig. 3b. This result indicates that I_{sym} is proportional to P_{in} , which is consistent with the scenario of the DC orbital pumping.

Figures 3a and 3b demonstrate that the sign of I_{sym} is reversed by reversing the magnetic field direction. This result is also consistent with the prediction of the orbital pumping because the DC component of the orbital polarization direction is reversed by reversing the magnetic field direction. We further studied the magnetic field angle θ dependence of the charge-current generation, as shown in Fig. 3c. By fitting the measured spectra, we plot I_{sym} with respect to θ for the Ni/Ti bilayer in Fig. 4a. As shown in Fig. 4a, the θ dependence of I_{sym} is well fitted by^{29,30,33,34}

$$I_{\text{sym}} = I_{\text{pump}} \cos^3 \theta + I_{\text{AMR}}^{\parallel} \sin 2\theta \cos \theta + I_{\text{AMR}}^{\perp} \sin 2\theta, \quad (2)$$

where I_{pump} arises from the spin or orbital pumping. $I_{\text{AMR}}^{\parallel}$ and I_{AMR}^{\perp} arise from the AMR due to in-plane and out-of-plane microwave magnetic fields, respectively. This result shows that the spin rectification signal in this system is dominated by the AMR because the PHE and AHE contributions show different angular dependences; the PHE contributions are proportional to $\cos 2\theta \cos \theta$ and $\cos 2\theta$ for in-plane and out-of-plane microwave magnetic fields, respectively, and the AHE contribution varies as $\cos \theta$ for an in-plane microwave magnetic field and is constant for an out-of-plane microwave magnetic field^{30,34}. Here, Eq. (2) indicates that I_{sym} at $\theta = 0$ corresponds to I_{pump} . The fitting result in Fig. 4a confirms that the I_{sym} component of the charge-current signal in the Ni/Ti bilayer at $\theta = 0$ varies as $\cos^3 \theta$, supporting that the charge-current signals shown in Fig. 2a arise from the orbital pumping. We also confirmed that the I_{pump} component is negligible in the Ni single-layer and the Fe/Ti bilayer, as shown in Figs. 4b and 4c. These results support that the generation of the charge current requires the IOHE of the Ti layer and the strong spin-orbit correlation of the Ni layer. Here, we note that I_{pump} is also observed in a Co/Ti bilayer (see Figs. 4d and 4e). The measured value of $I_{\text{pump}}/P_{\text{abs}}$ for the Co/Ti bilayer is smaller than that of the Ni/Ti bilayer but is larger than that of the Fe/Ti bilayer. This result is consistent with the model of the orbital pumping because the orbital response of Co is weaker than that of Ni but is stronger than that of Fe²⁰. For the Ni/Ti bilayer, we have further checked the

validity of the experiment by performing the pumping experiment in which the out-of-plane microwave magnetic field is dominant (see Supplementary Note 5). The magnetic damping is also investigated for the Ni/Ti bilayer (see Supplementary Note 6).

As a reference, we measured I_{DC} for a Fe(5 nm)/Pt(10 nm) bilayer, as shown in Figs. 4f and 4g. This result shows that the sign of I_{pump} in the Ni/Ti bilayer is the same as that in the Fe/Pt bilayer. In the Fe/Pt bilayer, the I_{pump} signal is dominated by the ISHE due to the spin pumping because of the weak spin-orbit correlation in the Fe layer and the strong ISHE in the Pt layer. In the scenario of the spin pumping, the spin polarization direction is defined by the magnetization direction and is independent of the choice of the FM layer³⁵. In contrast, the orbital polarization direction of the orbital current generated by the orbital pumping can depend on the sign of the spin-orbit correlation in the FM layer. In Ni, the spin-orbit correlation is positive, indicating that the direction of the orbital polarization of the orbital current is the same as that of the spin polarization of the spin current generated by the spin pumping¹⁴. Thus, the same sign of I_{pump} between the Ni/Ti and Fe/Pt bilayers indicates that the sign of the orbital Hall angle in the Ti layer is the same as that of the spin Hall angle in the Pt layer. This result is consistent with the theoretical prediction that the signs of the orbital Hall conductivity in Ti and the spin Hall conductivity in Pt are both positive³⁶, supporting that the observed signal in the Ni/Ti bilayer arises from the IOHE. We also note that the sign of the orbital torque in the Ni/Ti bilayer is the same as that of the spin torque produced by the SHE in Pt²².

To characterize the strength of the charge-current generation through the orbital pumping and IOHE, we define the conversion efficiency from the absorbed microwave power P_{abs} to the generated charge current I_{pump} as

$$\kappa = \frac{I_{\text{pump}}}{P_{\text{abs}}} \frac{\xi \gamma W M_s t_{\text{FM}} \sigma_{\text{NM}} \sqrt{(\mu_0 M_{\text{eff}}^2) + (4\pi f / \gamma)^2}}{2ef}, \quad (3)$$

where γ is the gyromagnetic ratio, e is the elementary charge, and ξ is a geometrical factor (for details, see Supplementary Note 2). t_{FM} , M_s , and M_{eff} are the thickness, saturation magnetization, and effective demagnetization field of the FM layer, respectively. σ_{NM} is the conductivity of the NM layer. Here, the conversion efficiency κ is defined such that it corresponds to $g_{\text{eff}}^{\uparrow\downarrow} \sigma_{\text{SHE}} \lambda_s \tanh(t_{\text{NM}} / 2\lambda_s)$ in the case where the charge current originates from the ISHE induced by the spin pumping, where $g_{\text{eff}}^{\uparrow\downarrow}$ is the effective spin mixing conductance, σ_{SHE} is the spin Hall conductivity, and λ_s is the spin diffusion length. In analogy to the spin

pumping, we expect that the charge current generated by the orbital pumping is determined by the orbital pumping efficiency β , the orbital Hall conductivity σ_{OHE} , and the orbital diffusion length λ_o , and therefore we use κ defined in Eq. (3) to characterize the strength of the orbital pumping and IOHE.

In Fig. 5, we show Ti-layer thickness t_{Ti} dependence of κ , determined by measuring the θ dependence of I_{DC} , for the Ni(5 nm)/Ti(t_{Ti}) bilayers. The charge-current generation efficiency κ of the Ni/Ti bilayer is about an order of magnitude smaller than $\kappa = 24 \times 10^{15} \text{ } \Omega^{-1}\text{m}^{-2}$ of the Fe(5 nm)/Pt(10 nm) bilayer, which is roughly consistent with the difference between the generation efficiencies of the orbital and spin torques in these systems²². Figure 5 shows that κ of the Ni/Ti bilayer increases with t_{Ti} . By fitting the t_{Ti} dependence of κ for the Ni/Ti bilayer with a function proportional to $\tanh(t_{\text{Ti}}/2\lambda_{\text{Ti}})$, we obtain the characteristic length of the charge-current generation to be $\lambda_{\text{Ti}} = 4.6 \text{ nm}$. This characteristic length is an order of magnitude smaller than that of the orbital-torque generation^{21,22}, implying that the length scale associated with the orbital transport triggered by the orbital pumping is different from that triggered by the OHE. Similar arguments have been made for spin transport; a potential difference in the length scales of diffusive spin currents and intrinsically generated spin Hall currents has been suggested, but their relationship remains unclear³⁷.

It is also worth noting the potential role of the inverse orbital Rashba-Edelstein effect in the charge-current generation induced by the orbital pumping. Recently, ultrafast dynamics of orbital transport have been studied using time-domain THz emission spectroscopy³⁸. In the experiment, the orbital transport is triggered by exciting a SiO₂/W/Ni film with femtosecond laser pulses. In the SiO₂/W/Ni film, the current-induced orbital torque, or the charge-to-orbital conversion, has been observed to be dominated by the OHE in the W layer²². However, the THz emission dynamics in the SiO₂/W/Ni film indicates that the orbital-to-charge conversion is dominated by the inverse orbital Rashba-Edelstein effect at the SiO₂/W interface. This finding suggests that the direct and inverse orbital responses could be dominated by the different mechanisms. The relatively short characteristic length observed for the orbital pumping suggests the possibility that the inverse orbital Rashba-Edelstein effect contributes to the charge-current generation. Understanding the length scales associated with orbital transport remains a challenge for future studies.

Conclusions and outlook

In conclusion, we have presented experimental evidence for the orbital pumping, where the precession of magnetization results in the emission of an orbital current into an adjacent layer. We have shown that the orbital current generated by the orbital pumping in the Ni/Ti bilayer is converted into a charge current through the IOHE in the Ti layer without using spin-orbit coupling. Although a recent study on $\text{Y}_3\text{Fe}_5\text{O}_{12}/\text{Pt}/\text{CuO}_x$ structures suggested the involvement of the inverse orbital Rashba-Edelstein effect in the generation of a charge current, the underlying mechanism is the spin pumping into the Pt layer and subsequent spin-to-orbital conversion by spin-orbit coupling in the Pt layer³⁹. This mechanism is distinct from the emission of orbital currents by the orbital pumping, observed in the present work.

The spin pumping is one of the most versatile and powerful mechanisms for spin-current generation, which enables spin injection into a wide variety of systems ranging from metals and semiconductors to magnetic insulators, organic materials, superconductors, and topological insulators^{9,10,40–43}. This exceptional ability of the spin pumping has played an important role in the discovery of a variety of fundamental phenomena in spintronics. We anticipate that the orbital pumping—the orbital counterpart of the spin pumping—provides a powerful way to explore the physics of orbital currents and orbital dynamics. Our results provide a fundamental piece of information for deeper understanding of the angular momentum dynamics in solids at the nanoscale, which will stimulate further experimental and theoretical studies.

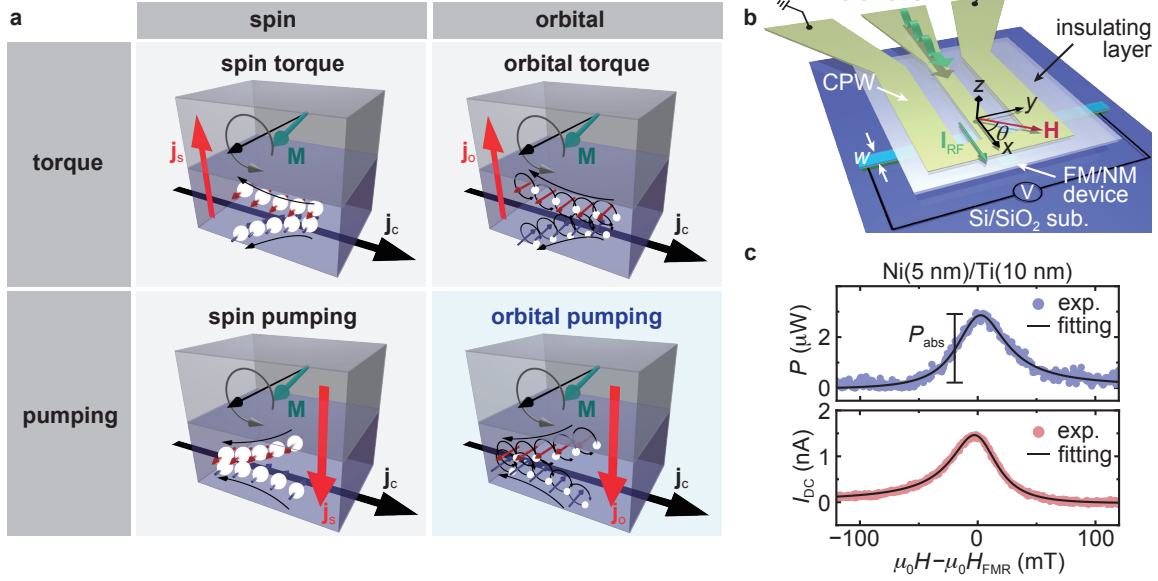


Figure 1. Orbital pumping and inverse orbital Hall effect. **a**, Schematic illustration of the spin torque, spin pumping, orbital torque, and orbital pumping. **b**, Schematic illustration of the experimental setup. **c**, Magnetic field H dependence of the microwave absorption intensity P (upper) and the charge current I_{DC} (lower) for the Ni(5 nm)/Ti(10 nm) bilayer measured at $\theta = 0$ with $f = 10$ GHz and $P_{in} = 10$ mW. The solid circles are the experimental data. The H dependence of I_{DC} is fitted with the sum of symmetric and antisymmetric functions (see the solid curve). The H dependence of P is fitted with the sum of symmetric and antisymmetric functions⁴⁴ (see the solid curve): $P = P_{abs}W^2 / [(\mu_0 H - \mu_0 H_{FMR})^2 + W^2] + P_{antisym}W(\mu_0 H - \mu_0 H_{FMR}) / [(\mu_0 H - \mu_0 H_{FMR})^2 + W^2]$.

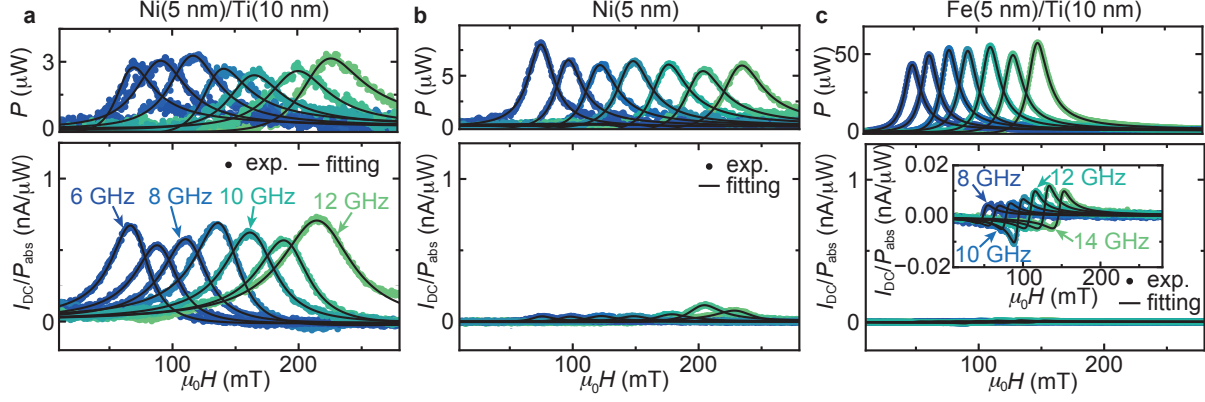


Figure 2. Role of Ti and FM layers in charge-current generation. a-c, Magnetic field H dependence of P and $I_{\text{DC}}/P_{\text{abs}}$ for (a) the Ni(5 nm)/Ti(10 nm) bilayer, (b) the Ni(5 nm) single-layer, and (c) the Fe(5 nm)/Ti(10 nm) bilayer measured at $\theta = 0$ and $P_{\text{in}} = 10$ mW. The frequency f of the RF current was varied from 6 GHz to 12 GHz in 1 GHz steps for the Ni/Ti and Ni films and from 8 GHz to 14 GHz in 1 GHz steps for the Fe/Ti film. The charge current is defined as $I_{\text{DC}} = V_{\text{DC}}/R$, and P_{abs} is the microwave absorption intensity at $H = H_{\text{FMR}}$ (see Fig. 1c). The solid circles are the experimental data, and the solid curves are the fitting result using the sum of symmetric and antisymmetric functions. The inset shows a magnified view of the signals.

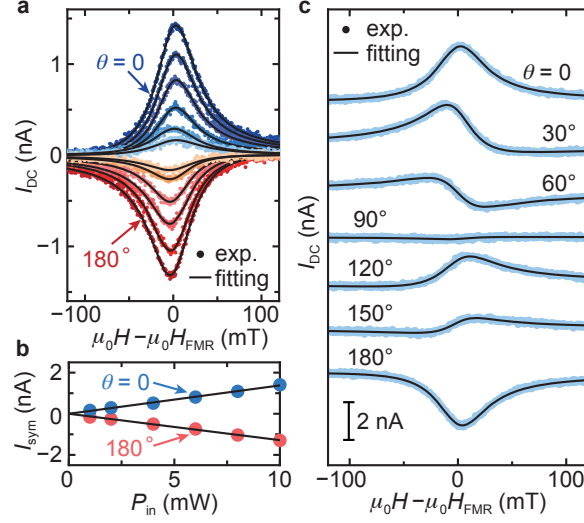


Figure 3. Charge-current spectra at various microwave powers and magnetic field angles. **a**, Magnetic field H dependence of I_{DC} for the Ni(5 nm)/Ti(10 nm) bilayer at $\theta = 0$ (blue) and $\theta = 180^\circ$ (red) measured with $f = 10$ GHz and different microwave powers $P_{in} = 1, 2, 4, 6, 8$ and 10 mW. The solid circles are the experimental data, and the solid curves are the fitting result using the sum of symmetric and antisymmetric functions. **b**, P_{in} dependence of I_{sym} for the Ni(5 nm)/Ti(10 nm) bilayer measured with $f = 10$ GHz at $\theta = 0$ (blue) and $\theta = 180^\circ$ (red). The solid circles are the experimental data, and the solid lines are the linear fitting result. **c**, H dependence of I_{DC} for the Ni(5 nm)/Ti(10 nm) bilayer at different in-plane magnetic field angle θ measured with $P_{in} = 10$ mW and $f = 10$ GHz.

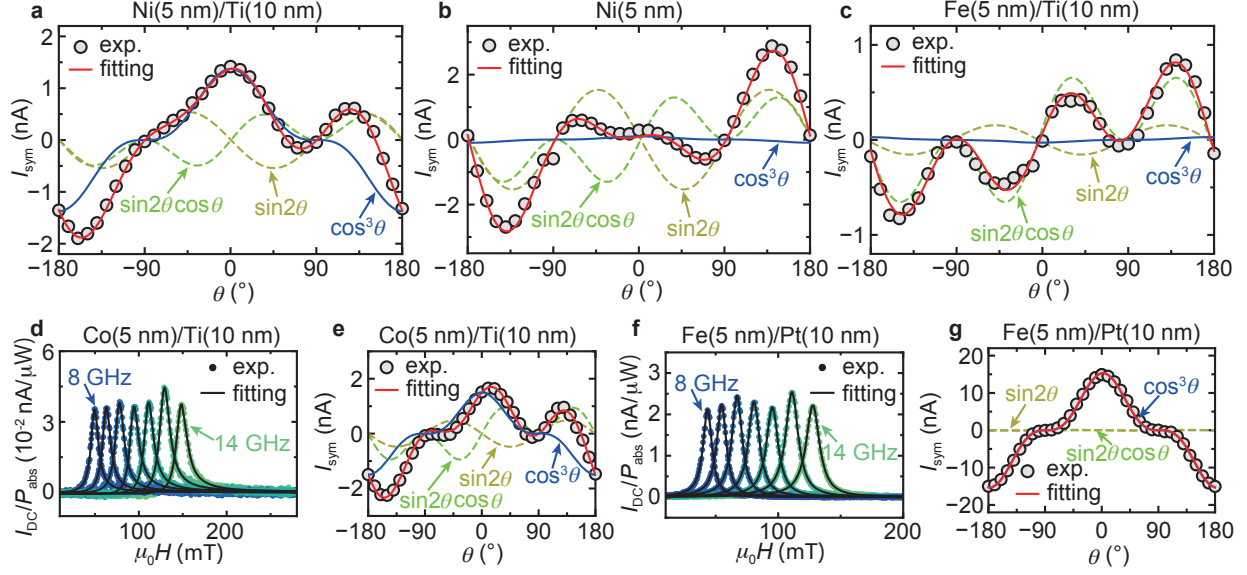


Figure 4. Magnetic-field angle dependence of charge current. a-c, In-plane magnetic field angle θ dependence of I_{sym} for (a) the Ni(5 nm)/Ti(10 nm) bilayer, (b) the Ni(5 nm) single-layer, and (c) the Fe(5 nm)/Ti(10 nm) bilayer at $f = 10$ GHz with $P_{\text{in}} = 10$ mW. The curves in red are the fitting result using Eq. (2), which is the sum of functions proportional to $\cos^3\theta$ (solid curves in blue), $\sin 2\theta \cos \theta$ (dashed curves in green), and $\sin 2\theta$ (dashed curves in yellow). d, H dependence of $I_{\text{DC}}/P_{\text{abs}}$ for the Co(5 nm)/Ti(10 nm) bilayer measured at $\theta = 0$ and $P_{\text{in}} = 10$ mW. The frequency f of the RF current was varied from 8 GHz to 14 GHz in 1 GHz steps. e, θ dependence of I_{sym} for the Co(5 nm)/Ti(10 nm) bilayer at $f = 10$ GHz. f, H dependence of $I_{\text{DC}}/P_{\text{abs}}$ for the Fe(5 nm)/Pt(10 nm) bilayer measured at $\theta = 0$ and $P_{\text{in}} = 1$ mW. The frequency f of the RF current was varied from 8 GHz to 14 GHz in 1 GHz steps. g, θ dependence of I_{sym} for the Fe(5 nm)/Pt(10 nm) bilayer at $f = 10$ GHz.

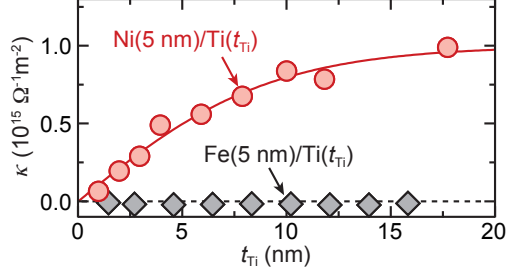


Figure 5. Charge-current generation efficiency. Ti-layer thickness t_{Ti} dependence of the charge-current generation efficiency κ , defined in Eq. (3), for the Ni(5 nm)/Ti(t_{Ti}) bilayers (red circles) and the Fe(5 nm)/Ti(t_{Ti}) bilayers (gray diamonds). The values of κ are determined from the I_{pump} and P_{abs} measured at $f = 10$ GHz, where I_{pump} is determined from the θ dependence of I_{DC} for each device. The solid curve in red is the fitting result using a function proportional to $\tanh(t_{\text{Ti}}/2\lambda_{\text{Ti}})$.

Methods

Device fabrication. The FM(5 nm)/NM(t_{NM}) bilayers (FM = Ni, Fe or Co, NM = Ti or Pt) were deposited on thermally oxidized Si substrates using radio frequency (RF) magnetron sputtering under a 6N-purity-Ar atmosphere at room temperature. The working pressure was 0.4 Pa. The thicknesses of the SiO₂ and Si layers are 100 nm and 625 μm , respectively. For the sputtering of the FM/Ti bilayers, the base pressure was better than 5×10^{-7} Pa, which was achieved by reducing the residual hydrogen and oxygen contents through a sputtering process using a Ti target (at least 0.4 Pa, 5 min, 120 W). The FM/Pt bilayers were sputtered with a base pressure better than 1.0×10^{-5} Pa. To vary the Ti-layer thickness of the Ni/Ti bilayer on the same substrate, a wedged Ti film was fabricated by using a linear shutter. All samples were capped by 4-nm-thick-SiO₂ to prevent oxidation. For the pumping measurement, the films were fabricated into Hall cross structures with a width of $w = 8 \mu\text{m}$ utilizing the conventional photolithography with negative resist followed by the Ar-ion milling and lift-off technique. The device was placed under a coplanar waveguide (CPW) consisting of Ti(3 nm)/Au(400 nm) deposited by RF magnetron sputtering. A SiO₂(170 nm) insulating layer was deposited by RF magnetron sputtering between the device and the CPW.

Microwave absorption and voltage measurements. For the FM/NM bilayers, we measured DC electromotive force V_{DC} using a nanovoltmeter (2182A, Keithley) with applying an RF current to the CPW and in-plane magnetic field H . The in-plane magnetic field H was applied at an angle of θ from the direction of the applied RF current (see Fig. 1b). The microwave absorption intensity P was determined by measuring S_{11} using a vector network analyzer (VNA) (N5222A, Keysight)⁴⁵, where $P = (\Delta|S_{11}|^2/|S_{11}^0|)P_{\text{in}}$. Here, $|S_{11}^0|$ represents the reflection loss between the CPW and the port of the VNA without the FMR, and $\Delta|S_{11}|^2$ is the change ratio of the reflected microwave power at the FMR (see Supplementary Note 2).

Data availability

The data that support the findings of this study are available from the corresponding author upon reasonable request.

References

- ¹ Maekawa, S., Valenzuela, S. O., Saitoh, E. & Kimura, T. (eds.) *Spin Current* (Oxford University Press, Oxford, 2012).
- ² Manchon, A. *et al.* Current-induced spin-orbit torques in ferromagnetic and antiferromagnetic systems. *Rev. Mod. Phys.* **91**, 035004 (2019).
- ³ Ryu, J., Lee, S., Lee, K.-J. & Park, B.-G. Current-induced spin-orbit torques for spintronic applications. *Adv. Mater.* **32**, 1907148 (2020).
- ⁴ Hirohata, A. *et al.* Review on spintronics: Principles and device applications. *J. Magn. Magn. Mater.* **509**, 166711 (2020).
- ⁵ Dieny, B. *et al.* Opportunities and challenges for spintronics in the microelectronics industry. *Nat. Electron.* **3**, 446–459 (2020).
- ⁶ Mizukami, S., Ando, Y. & Miyazaki, T. Effect of spin diffusion on Gilbert damping for a very thin permalloy layer in Cu/permalloy/Cu/Pt films. *Phys. Rev. B* **66**, 104413 (2002).
- ⁷ Tserkovnyak, Y., Brataas, A. & Bauer, G. E. W. Enhanced Gilbert damping in thin ferromagnetic films. *Phys. Rev. Lett.* **88**, 117601 (2002).
- ⁸ Tserkovnyak, Y., Brataas, A., Bauer, G. E. W. & Halperin, B. I. Nonlocal magnetization dynamics in ferromagnetic heterostructures. *Rev. Mod. Phys.* **77**, 1375 (2005).
- ⁹ Kajiwara, Y. *et al.* Transmission of electrical signals by spin-wave interconversion in a magnetic insulator. *Nature* **464**, 262–266 (2010).
- ¹⁰ Wang, H., Du, C., Hammel, P. C. & Yang, F. Antiferromagnonic spin transport from $\text{Y}_3\text{Fe}_5\text{O}_{12}$ into NiO. *Phys. Rev. Lett.* **113**, 097202 (2014).
- ¹¹ Noël, P. *et al.* Non-volatile electric control of spin-charge conversion in a SrTiO_3 Rashba system. *Nature* **580**, 483–486 (2020).
- ¹² Go, D., Jo, D., Lee, H.-W., Kläui, M. & Mokrousov, Y. Orbitronics: Orbital currents in solids. *EPL* **135**, 37001 (2021).
- ¹³ Kim, J. & Otani, Y. Orbital angular momentum for spintronics. *J. Magn. Magn. Mater.* **563**, 169974 (2022).
- ¹⁴ Go, D. & Lee, H.-W. Orbital torque: Torque generation by orbital current injection. *Phys.*

- Rev. Research* **2**, 013177 (2020).
- ¹⁵ Chen, X. *et al.* Giant antidamping orbital torque originating from the orbital Rashba-Edelstein effect in ferromagnetic heterostructures. *Nat. Commun.* **9**, 2569 (2018).
- ¹⁶ Kim, J. *et al.* Nontrivial torque generation by orbital angular momentum injection in ferromagnetic-metal/Cu/Al₂O₃ trilayers. *Phys. Rev. B* **103**, L020407 (2021).
- ¹⁷ Tazaki, Y. *et al.* Current-induced torque originating from orbital current. *arXiv:2004.09165* (2020).
- ¹⁸ Ding, S. *et al.* Harnessing orbital-to-spin conversion of interfacial orbital currents for efficient spin-orbit torques. *Phys. Rev. Lett.* **125**, 177201 (2020).
- ¹⁹ Lee, S. *et al.* Efficient conversion of orbital Hall current to spin current for spin-orbit torque switching. *Commun. Phys.* **4**, 234 (2021).
- ²⁰ Lee, D. *et al.* Orbital torque in magnetic bilayers. *Nat. Commun.* **12**, 6710 (2021).
- ²¹ Choi, Y.-G. *et al.* Observation of the orbital Hall effect in a light metal Ti. *Nature* **619**, 52–56 (2023).
- ²² Hayashi, H. *et al.* Observation of long-range orbital transport and giant orbital torque. *Commun. Phys.* **6**, 32 (2023).
- ²³ Sala, G. & Gambardella, P. Giant orbital Hall effect and orbital-to-spin conversion in 3*d*, 5*d*, and 4*f* metallic heterostructures. *Phys. Rev. Research* **4**, 033037 (2022).
- ²⁴ Go, D. *et al.* Orbital pumping by magnetization dynamics in ferromagnets. *arXiv:2309.14817* (2023).
- ²⁵ Go, D. *et al.* Theory of current-induced angular momentum transfer dynamics in spin-orbit coupled systems. *Phys. Rev. Research* **2**, 033401 (2020).
- ²⁶ Du, C., Wang, H., Yang, F. & Hammel, P. C. Systematic variation of spin-orbit coupling with *d*-orbital filling: Large inverse spin Hall effect in 3*d* transition metals. *Phys. Rev. B* **90**, 140407 (2014).
- ²⁷ Saitoh, E., Ueda, M., Miyajima, H. & Tatara, G. Conversion of spin current into charge current at room temperature: Inverse spin-Hall effect. *Appl. Phys. Lett.* **88**, 182509 (2006).
- ²⁸ Ando, K. *et al.* Inverse spin-Hall effect induced by spin pumping in metallic system. *J. Appl. Phys.* **109**, 103913 (2011).
- ²⁹ Harder, M., Cao, Z. X., Gui, Y. S., Fan, X. L. & Hu, C.-M. Analysis of the line shape of electrically detected ferromagnetic resonance. *Phys. Rev. B* **84**, 054423 (2011).

- ³⁰ Iguchi, R. & Saitoh, E. Measurement of spin pumping voltage separated from extrinsic microwave effects. *J. Phys. Soc. Jpn.* **86**, 011003 (2017).
- ³¹ Flovik, V., Macià, F., Kent, A. D. & Wahlström, E. Eddy current interactions in a ferromagnet-normal metal bilayer structure, and its impact on ferromagnetic resonance lineshapes. *J. Appl. Phys.* **117**, 143902 (2015).
- ³² Chuang, T. C., Su, P. L., Wu, P. H. & Huang, S. Y. Enhancement of the anomalous Nernst effect in ferromagnetic thin films. *Phys. Rev. B* **96**, 174406 (2017).
- ³³ Zhou, H. *et al.* Spatial symmetry of spin pumping and inverse spin Hall effect in the Pt/Y₃Fe₅O₁₂ system. *Phys. Rev. B* **94**, 134421 (2016).
- ³⁴ Harder, M., Gui, Y. & Hu, C.-M. Electrical detection of magnetization dynamics via spin rectification effects. *Phys. Rep.* **661**, 1–59 (2016).
- ³⁵ Yoshino, T. *et al.* Universality of the spin pumping in metallic bilayer films. *Appl. Phys. Lett.* **98**, 132503 (2011).
- ³⁶ Salemi, L. & Oppeneer, P. M. First-principles theory of intrinsic spin and orbital Hall and Nernst effects in metallic monoatomic crystals. *Phys. Rev. Materials* **6**, 095001 (2022).
- ³⁷ Amin, V. P., Haney, P. M. & Stiles, M. D. Interfacial spin-orbit torques. *J. Appl. Phys.* **128**, 151101 (2020).
- ³⁸ Seifert, T. S. *et al.* Time-domain observation of ballistic orbital-angular-momentum currents with giant relaxation length in tungsten. *Nat. Nanotechnol.* (2023). URL <https://doi.org/10.1038/s41565-023-01470-8>.
- ³⁹ Santos, E. *et al.* Inverse orbital torque via spin-orbital intertwined states. *Phys. Rev. Appl.* **19**, 014069 (2023).
- ⁴⁰ Ando, K. *et al.* Electrically tunable spin injector free from the impedance mismatch problem. *Nat. Mater.* **10**, 655–659 (2011).
- ⁴¹ Watanabe, S. *et al.* Polaron spin current transport in organic semiconductors. *Nat. Phys.* **10**, 308–313 (2014).
- ⁴² Jeon, K.-R. *et al.* Enhanced spin pumping into superconductors provides evidence for superconducting pure spin currents. *Nat. Mater.* **17**, 499–503 (2018).
- ⁴³ Shiomi, Y. *et al.* Spin-electricity conversion induced by spin injection into topological insulators. *Phys. Rev. Lett.* **113**, 196601 (2014).
- ⁴⁴ Gupta, S. *et al.* Broadband strip-line ferromagnetic resonance spectroscopy of soft magnetic

CoFeTaZr patterned thin films. *AIP Adv.* **8**, 056125 (2018).

- ⁴⁵ Iguchi, R. *et al.* Spin pumping without three-magnon splitting in polycrystalline Bi₁Y₂Fe₅O₁₂/Pt bilayer structure. *Jpn. J. Appl. Phys.* **51**, 103004 (2012).

Correspondence and requests for materials should be addressed to K.A. (ando@appi.keio.ac.jp)

Acknowledgements

This work was supported by JSPS KAKENHI (Grant Number: 22H04964, 20H00337, 20H02593, 23K19037), Spintronics Research Network of Japan (Spin-RNJ), and MEXT Initiative to Establish Next-generation Novel Integrated Circuits Centers (X-NICS) (Grant Number: JPJ011438). H.H. is supported by JSPS Grant-in-Aid for Research Fellowship for Young Scientists (DC1) (Grant Number 20J20663). D.G. and Y.M. acknowledge Deutsche Forschungsgemeinschaft (DFG, German Research Foundation) - TRR 173/2 - 268565370 - Spin+X (Project A11), and TRR 288 - 422213477 (Project B06), for funding.

Competing interest

The authors declare no competing interests.

Author contributions

H.H. fabricated devices, collected and analyzed the data, and performed the materials characterization. H.H. and K.A. designed the experiments. H.H., D.G., Y.M., and K.A. developed the explanation. H.H. and K.A. wrote the manuscript with the help from D.G and Y.M. All authors discussed results and reviewed the manuscript. K.A. supervised the study.